

# Magnetic Pinching of Hyperbolic Flux Tubes: I. Basic Estimations

V.S. Titov

*Theoretische Physik IV, Ruhr-Universität Bochum, 44780 Bochum*

st@tp4.ruhr-uni-bochum.de

and

K. Galsgaard and T. Neukirch

*School of Mathematics and Statistics, University of St Andrews, St Andrews KY16 9SS,  
Scotland*

## ABSTRACT

The concept of hyperbolic flux tubes (HFTs) is a generalization of the concept of separator field lines for coronal magnetic fields with a trivial magnetic topology. An effective mechanism of a current layer formation in HFTs is proposed. This mechanism is called magnetic pinching and it is caused by large-scale shearing motions applied to the photospheric feet of HFTs in a way as if trying to twist the HFT. It is shown that in the middle of an HFT such motions produce a hyperbolic flow that causes an exponentially fast growth of the current density in a thin force-free current layer. The magnetic energy associated with the current layer that is built up over a few hours is sufficient for a large flare. Other implications of HFT pinching for solar flares are discussed as well.

*Subject headings:* solar flares: current sheets, magnetic reconnection

## 1. INTRODUCTION

Over the last decades it has become clear from both observational and theoretical points of view that current sheet formation in the corona is one of the key processes for solar physics (Parker 1994; Priest & Forbes 2000). In particular, it provides a temporary deposit around

the current sheets of free magnetic energy for solar flares and creates favorable conditions for subsequent rapid conversion of this energy into other forms. The corresponding local growth of current density in the current sheet formation process may stimulate the onset of plasma instabilities and the development of anomalous resistivity. Turbulent dissipation of the current layer due to such instabilities is thought to be a reason of thermal and supra-thermal processes in solar flares (Somov 1992).

Typically, the coronal magnetic field is frozen into plasma and its Maxwellian stresses are large enough to dominate over other forces in active regions. This means that in such plasmo-magnetic configurations the magnetic pressure and tension approximately balance each other. Also the transit time of perturbations through the corona is much less than the characteristic time of photospheric motions. Therefore, the configurations have to evolve through a sequence of nearly force-free equilibria in response to the time variation of the photospheric boundary conditions. Due to the frozen-in condition the topological structure of the magnetic field in the corona is not changed by horizontal photospheric motions. However, it may be changed by a vertical injection of a new magnetic flux through the photosphere. In the generic case this may lead to the appearance of magnetic null points in the corona. The magnetic forces in the vicinity of the nulls are too weak to withstand to large variations of the ambient magnetic stress. Therefore, the corresponding neighborhoods of the nulls generally collapse in evolving fields, producing topologically accessible current singularities (Priest & Titov 1996).

Similar processes have to occur in the vicinity of the so-called bald patches (Titov et al. 1993), which are those segments of photospheric polarity inversion lines (IL), where the field lines touch the photosphere (Seehafer 1986). In comparison with the case of the nulls the physics of the formation of the current singularities is a bit different here: the current sheets are formed due to an “attachment” of the touching field lines to the very heavy photospheric material (Low 1987; Aly & Amari 1989; Vekstein et al. 1991).

Thus, the presence of the topological features such as null points and bald patches is a *condition* for the formation of current singularities in coronal configurations. An analysis of magnetic field structures in solar flares shows, however, that not all the observed event can be explained by the presence of such topological features and that therefore this class of features has to be extended (Démoulin et al. 1997). A possible extension can be found by using the concept of field line connectivity. Indeed, in the framework of this approach the nulls and bald patches, as well as the separatrix field lines emanating from them, can be detected by discontinuous jumps of the field line connectivity. The desired extension then can be found by weakening the condition that the jump in connectivity is discontinuous to requiring only that the field line connectivity exhibits a “large” spatial variation (Seehafer

1986; Longcope & Strauss 1994). The flux tubes which exhibit such a behavior are called quasi-separatrix layers (QSLs) (Priest & Démoulin 1995). It should be emphasized that QSLs are geometrical objects rather than topological ones, since they can be removed by suitable continuous deformations of the magnetic field (Titov & Hornig 2002). The genuine separatrix lines and surfaces are degenerate or limiting cases of QSLs (Titov et al. 2002).

For determining QSLs in a given magnetic field a measure of magnetic connectivity is required. The proper measure is *the degree of squashing* of elemental flux tubes, which connect opposite photospheric polarities and have infinitesimal cross-sections (Titov et al. 1999). A QSL is then defined as a flux tube with abnormally large values of the squashing degree. In application to quadrupole magnetic configurations formed by two bipolar groups of sunspots this criterion reveals a special geometrical feature called *hyperbolic flux tube* (HFT) (Titov et al. 2002). HFTs can be understood as a combination of two intersecting QSLs. In the limiting case, where the sunspot flux is concentrated in point-like sources, the HFT collapses into two separatrix surfaces intersecting along a separator field line. The separator is a field line connecting two null points which appear in this limiting case and it is a favorable site for current sheet formation caused by displacements of the sunspot positions (Sweet 1969; Gorbachev & Somov 1988; Lau & Finn 1990; Longcope 2002). Therefore it is natural to expect that HFTs are also preferred sites for current sheet formation. Here we will call such a process of current sheet formation in an HFT *magnetic pinching*, by analogy with a similar process studied in axisymmetric laboratory plasmas (the corresponding similarity will be further clarified below).

It is the purpose of this series of papers to understand and quantify the basic properties of the process of current sheet formation in HFTs. In the present paper we present basic theoretical calculations and estimates relevant to this problem in the following way. In § 2 the problem and an idea for its solution are formulated. In § 3 a simplified quadrupole configuration used to model an HFT is described. In § 4 a kinematic model of the HFT pinching process is developed. In § 5 this model is improved by incorporating an approximate form of magnetic force balance. In § 6 the implications of the obtained results for solar flares are discussed. Section 7 presents the conclusions of this work. The results of dynamic and quasi-static simulations of the HFT pinching process will be described in forthcoming papers of this series.

## 2. FORMATION OF A CURRENT LAYER IN A QUADRUPOLE CONFIGURATION

It is clear that the pinching of an HFT has to be due to some photospheric boundary conditions, which in the simplest form imply certain footpoint displacements of the field lines on the photosphere. Priest & Démoulin (1995) proposed that all types of displacements across QSLs must lead to the formation of a current layer. However, there are both theoretical arguments (Inverarity & Titov 1997) and numerical simulations (Galsgaard 2000) which indicate that this is not the case – the footpoint displacements must be of a special type to cause the formation of current layers. As HFTs consist of intersecting QSLs it is to be expected that this result also has some importance for the pinching of HFTs.

To gain a better understanding of the problem of finding those footpoint displacements which give rise to the pinching of HFTs, we first briefly discuss a particular aspect of the phenomenology of large flares. It was discovered a long time ago (Martres et al. 1966; Moreton & Severny 1968) that such flares often occur in the vicinity of S-shaped ILs. On the basis of a potential field model using point sources Gorbachev & Somov (1988) proposed that this fact actually implies the appearance of a current sheet forming along a separator field line. The subsequent instability of this current sheet results in a large flare. In a quadrupole configuration this process is driven by suitable vortex motions near the IL. As we will show below this idea also works, under suitable modifications, if one replaces the separator field line by an HFT.

It is important to notice that in a realistic configuration with distributed photospheric flux the appearance of a separator in the corona is quite problematic, because it requires the simultaneous appearance of two magnetic nulls in the corona. For the presence of an HFT, however, much less restrictive conditions apply, so that it is a generic geometrical feature for quadrupole configurations (Titov et al. 2002).

The structure of a typical HFT is shown in Figure 1a. Along an HFT its cross-section typically changes as shown in the following schematic sketch

$$/ \rightarrow \times \rightarrow \times \rightarrow \times \rightarrow \backslash.$$

The intersections of the HFT with the photosphere have a crescent-like shape with the tips of the crescents located inside the neighbouring sunspots of the same polarity. Thus, the photospheric field strength has minima in the middle of the crescents and increases significantly towards its tips. One footpoint of any field line inside the HFT is always close to one of the tips, while the other footpoint is in the middle of the opposite polarity crescent. In other words, each field line inside the HFT connects regions of strong and weak photospheric field of opposite polarity. Along each field line the field strength and the

Maxwellian stresses increase or decrease monotonically, depending on the direction of the field line from weak to strong field or vice versa. Towards the strong field region field lines will be relatively rigid becoming more flexible towards the weaker field region. In Figure 1a this property is depicted by the corresponding variation of the field line thickness.

Such a variation of field line rigidity within the HFT predetermines the structure of the three-dimensional deformation caused by displacements of the foot points. One can expect that the farther the field line remains inflexible from its rigid end, the farther the photospheric displacement from this end propagates into the corona. This implies, in particular, that a shearing motion across the crescent-like foot of the HFT easily propagates to its middle part in the corona. The same is true, of course, for the second foot. Since the cross-section of the HFT in its middle has an X-like shape, the shears propagating from the feet to the middle will superpose there perpendicular to each other. If the foot point motions at the feet are applying twist to the HFT, then their superposition will cause a hyperbolic flow pattern in the centre of the HFT (Figure 1b). Photospheric shearing motions are caused quite naturally by sunspot displacements perpendicular to the HFT feet and the twisting type of shearing motion corresponds exactly to the above mentioned S-like deformation of the IL by photospheric flows. Thus, the hyperbolic flow pattern in the middle of the HFT will persist as long as such sunspot displacements continue. As we will show this hyperbolic flow pattern causes an exponentially fast deformation of the HFT into a sheet-like structure (see below). Therefore, if the total length of the foot point displacements is comparable with the size of the active region one can expect a very large pinching of the middle part of the HFT due to the hyperbolic flow pattern.

We conclude that a combination of twisting foot point displacements perpendicular to the foot points of the HFT is sufficient for the formation of a strong current layer in the HFT. In this case the velocity field and transverse magnetic field component inside the HFT will have a similar hyperbolic structure but are inclined by  $45^\circ$  with respect to each other. In the theory of two-dimensional (2D) reconnection these hyperbolic structures of the velocity and magnetic field are the main prerequisites for the so-called magnetic collapse (Priest & Forbes 2000) or the dynamic formation of a current sheet (Syrovatskii 1981). The idea that current layers can form in three-dimensional (3D) magnetic configurations under the action of hyperbolic flows was also considered earlier. Galsgaard & Nordlund (1996) imposed two shearing motions of a fixed duration, one after another in mutually perpendicular directions, onto an initially uniform magnetic field. This forced the magnetic field lines to twist around each other, so that the magnetic tension stress appearing in this process sets up a stagnation flow halfway between the driving boundaries. The action of this flow during the corresponding time interval led to the formation of a strong current layer. To form such current layers Cowley et al. (1997) assumed the presence of stagnation

flows on the photosphere driving the system. However, sustaining these flows for sufficiently long time seems to be rather problematic. On the contrary, the twisting shears discussed above appear as a result of the appropriate displacements of the sunspots perpendicular to the HFT feet and can be part of the natural photospheric motions having a relatively long lifetime. Due to these arguments the hyperbolic flows generated inside an HFT are generic features of HFTs just as HFTs themselves are for quadrupolar magnetic field configurations.

### 3. AN HFT IN A SIMPLIFIED QUADRUPOLE CONFIGURATION

To facilitate the quantitative investigation of the problem, we simplify the quadrupole configuration discussed above in the same way as it is usually done to model magnetic flux braiding (Parker 1972). We assume that the coronal plasma and field are contained between two planes,  $z = -L$  and  $z = L$ , representing positive and negative photospheric polarities, respectively. Let the initial magnetic field be current-free and produced by four fictive magnetic charges placed outside of the model volume. The sources are all equal in strength but the four sources fall in two pairs which differ in polarity. The negative and positive pairs are located at the points  $\mathbf{r}_{1,3} = (\pm l, 0, L + d)$  and  $\mathbf{r}_{2,4} = (0, \pm l, -L - d)$ , respectively. Their strength is chosen to be  $B_s d^2$ , so that the normal component of the field at the photosphere would have extrema  $\approx \pm B_s$  when their depths are small ( $d \ll l, L$ ). Then the resulting initial magnetic field is given by

$$\mathbf{B}_0(\mathbf{r}) = B_s d^2 \sum_{n=1}^4 (-1)^n \frac{(\mathbf{r} - \mathbf{r}_n)}{|\mathbf{r} - \mathbf{r}_n|^3}. \quad (1)$$

This field has a trivial topological structure in the corona, since there are no nulls in the coronal volume  $|z| < L$ . However, owing to the presence of two flux concentrations in each photospheric plane (cf. Figure 2a and 2c) the geometry of the field is not simple in general. Such concentrations are smoothed out by a large expansion of the flux tubes between the planes to yield a rather homogeneous  $B_{0z}$ -distribution in the midplane  $z = 0$  (Figure 2b). The pairs of concentrations have an orientation which is perpendicular to each other and therefore the transverse field ( $B_{0x}, B_{0y}$ ) remains inhomogeneous in the plane  $z = 0$  and has the typical structure of a hyperbolic magnetic X-point (Figure 2b).

This allows us to approximate the magnetic field near this plane by

$$\mathbf{B}_0 \simeq (hx, -hy, B_{\parallel}), \quad (2)$$

where the gradient of the transverse field,  $h$ , and the longitudinal field,  $B_{\parallel}$ , are easily derived

from (1) to yield

$$h = \frac{6(B_s/L)\bar{d}^2\bar{l}^2}{[\bar{l}^2 + (1 + \bar{d})^2]^{5/2}}, \quad (3)$$

$$B_{\parallel} = \frac{4B_s\bar{d}^2(1 + \bar{d})}{[\bar{l}^2 + (1 + \bar{d})^2]^{3/2}}. \quad (4)$$

The bar over the length scales denotes their normalization to  $L$ . This approximation is fairly accurate for  $r, |z| \lesssim l$  and will be useful for our further analysis of the problem.

This configuration is constructed in such a way that it represents a simplified or “straightened” version of the HFT considered in the previous section. If we use the squashing degree of elemental flux tubes in QSLs as proposed by Titov et al. (1999),

$$Q = \frac{\left(\frac{\partial X_-}{\partial x_+}\right)^2 + \left(\frac{\partial X_-}{\partial y_+}\right)^2 + \left(\frac{\partial Y_-}{\partial x_+}\right)^2 + \left(\frac{\partial Y_-}{\partial y_+}\right)^2}{\left|\frac{\partial X_-}{\partial x_+} \frac{\partial Y_-}{\partial y_+} - \frac{\partial X_-}{\partial y_+} \frac{\partial Y_-}{\partial x_+}\right|}, \quad (5)$$

where the functions  $X_-(x_+, y_+)$  and  $Y_-(x_+, y_+)$  represent the connection between the field line footpoints  $((x_+, y_+)$  and  $(x_-, y_-)$ ), the surface of the HFT is defined by the condition  $Q = \text{const}$  with the constant  $\gg 2$ .

The value  $Q$  is invariant to interchanging the  $+$  and  $-$  signs in (5). A general way to compute  $Q$  numerically is to calculate field lines starting at neighboring footpoints and follow them to their other footpoints. Then the respective derivatives in (5) can be calculated. A sketch of the typical shape of the surface enclosing the HFT is presented in Figure 3a, which shows that the intersection of the HFT with the photospheric planes is very narrow in one direction and elongated in the other, connecting the two flux concentrations. The surfaces calculated using other values of  $Q$  have similar shapes and are nested inside each other with the corresponding value of  $Q$  growing as the surfaces approach the  $z$ -axis. The magnitudes of the magnetic field and the Maxwellian stresses in this “straightened” HFT are distributed in a similar way as in the more realistic curved HFT version described above.

To estimate the range of parameters for which the HFT is present, we calculate the maximum of  $Q$  within the configuration. To do this we start by noticing that if we extend our model magnetic field (1) to the region outside the model volume, then the  $z$ -axis coincides with a separator field line for this extended field because it has two null points on the  $z$ -axis outside the model volume (Figure 3b). Therefore, by construction, the maximum of  $Q$  inside the model volume is attained on the field line coinciding with the  $z$ -axis. In the following, we call this field line the *quasi-separator* and denote the corresponding squashing degree by

$Q_{\text{qs}}$ . Details of the derivation of  $Q_{\text{qs}}$  are given in Appendix A, with the result being

$$Q_{\text{qs}} = 2 \cosh 2\lambda, \quad (6)$$

where

$$\lambda = \int_{-L}^{+L} \left( \frac{\partial B_{0x}}{\partial x} / B_{0z} \right) \Big|_{\mathbf{r}=(0,0,z)} dz. \quad (7)$$

Thus,  $Q_{\text{qs}}$  grows exponentially with  $\lambda$ , which in turn grows if the gradient of the transverse field component increases and/or the longitudinal component decreases on average along the quasi-separator. The explicit form of the integrand in (7) is cumbersome but easily derivable from (1). Since the integral itself is not expressible in terms of elementary or special functions, we do not give further details of the integrand and simply present the corresponding numerical results of the integration in Figure 4. It can be seen that  $Q_{\text{qs}}$  strongly grows with a growing concentration of flux in the sunspots (i.e. decreasing  $d/L$ ) and if the distance of the sunspots of the same polarity decreases (i.e. decreasing  $l/L$ ). In other words, the stronger and the closer the sunspots in our configuration are, the larger will be the squashing degree  $Q_{\text{qs}}$  at the quasi-separator. Figure 4 of  $Q_{\text{qs}}$  indicates that the HFT should exist in this configuration for a relatively large range of parameters of the model.

#### 4. KINEMATICS OF HFT PINCHING

For the time scale during which the sunspots are passing each other, the flow velocity can be assumed to be constant and uniform in their vicinity. Between two spots moving in opposite directions a region of shearing flow must exist to provide a continuous velocity field. We restrict ourselves to the cases, where the spots of the same polarity move perpendicularly to the HFT feet. Taking for simplicity the characteristic velocity  $V_s$  to be the same for all spots, we define the photospheric velocity field by

$$\mathbf{v}_+ = V_s \tanh(y/l_{\text{sh}}) \hat{\mathbf{x}} \quad \text{at } z = -L \quad (8)$$

and

$$\mathbf{v}_- = \mp V_s \tanh(x/l_{\text{sh}}) \hat{\mathbf{y}} \quad \text{at } z = L, \quad (9)$$

where  $l_{\text{sh}}$  is a characteristic length scale of the shear, and we have kept the possibility to change the sign of the second velocity field to demonstrate the effects of favorable and unfavorable foot point motions (see below). Assuming that the shearing motions approximately



match the corresponding motions of the spots at the locations where  $B_z^2 \approx B_s^2/2$ , we can estimate  $l_{\text{sh}}$  at  $d < l$  as

$$l_{\text{sh}} \approx l - 0.6 d. \quad (10)$$

Depending on the sign ( $-$  or  $+$ ) in (9), we either have a “turning” or a “twisting” pair of shearing motions, respectively, which are applied to the feet of the HFT. It is crucial for our understanding of the pinching process of the HFT to consider these two fundamental cases. More general motions of the spots can be obtained as linear combinations of these two.

As discussed above, inside the photospheric boundaries the magnetic field strength grows from the middle of the HFT feet towards their ends which are located at the magnetic flux concentrations. Also field lines belonging to the HFT always connect regions of strong and weak magnetic field. Since the rigidity of the field lines is proportional to the local field strength, the HFT field lines are rigid at one footpoint and flexible at the other. These elastic properties of the HFT magnetic field strongly suggest that the effect of the photospheric shearing motion must propagate along the field lines from one boundary to the other but with gradually vanishing amplitude. We approximately model the resulting three-dimensional velocity field by extrapolating both (8) and (9) linearly into the volume and then superposing them with the result

$$\mathbf{v} = \frac{V_s}{2} \left[ \left(1 - \frac{z}{L}\right) \tanh\left(\frac{y}{l_{\text{sh}}}\right) \hat{\mathbf{x}} \mp \left(1 + \frac{z}{L}\right) \tanh\left(\frac{x}{l_{\text{sh}}}\right) \hat{\mathbf{y}} \right]. \quad (11)$$

This velocity field yields the simplest model for infinitesimal deformations ( $\mathbf{v} dt$ ) of the HFT over an infinitesimal time interval  $dt$  in response to the “turning” or “twisting” pair of photospheric shearing motions  $\mathbf{v}_+ dt$  and  $\mathbf{v}_- dt$ . The sign ( $-$  or  $+$ ) of the second term of (11) corresponds to “turning” or “twisting” motion, respectively. The velocity fields (11) are not exact solutions of the MHD equations, of course. Nevertheless, they are qualitatively consistent with the elastic properties of the HFT and hence studying the effect of these velocity fields provides useful insights into the physical mechanism of the HFT pinching process.

With this purpose we now investigate the effect of finite deformations of the HFT by the velocity fields (11). Finite deformations are described by the vector function  $\mathbf{r}(t, \mathbf{r}_0)$  in which  $\mathbf{r}_0 \equiv (x_0, y_0, z_0)$  represents the Lagrangian coordinates of plasma elements. This function  $\mathbf{r}(t, \mathbf{r}_0)$  is obtained from (11) by integrating the equation

$$\frac{d\mathbf{r}}{dt} = \mathbf{v} \quad (12)$$

with the initial condition  $\mathbf{r}(0, \mathbf{r}_0) = \mathbf{r}_0$ . Since the velocity fields (11) have a vanishing  $z$ -component, the corresponding deformations have only  $x$ - and  $y$ -components and the plasma

elements remain in the same plane  $z = \text{const}$  in which they were initially. It is of particular interest to study these deformations in the midplane  $z = 0$ , where the transverse magnetic field has a structure typical for the neighborhood of an X-point.

We have done this by computing the corresponding distortion of an initially uniform grid of plasma elements for two subsequent moments. The results are represented in Figure 5, which shows that “turning” shearing motions cause only a relatively slight distortion of the grid even if the sunspots move over distances of the order of  $L$ . The middle part of the HFT in this case just turns as a whole by an angle of  $\sim t$  with only modest changes in the sizes of the grid cells. By contrast, the “twisting” shearing motions produce a much stronger effect in the central parts of the grid causing an extreme squashing of the grid cells in one direction. The reason for this difference becomes clear if one compares the corresponding velocity fields in the plane  $z = 0$ . In the first case the velocity field has the typical structure of rotational flows (see Figure 6a), while in the second case it shows the velocity field of a stagnation point (Figure 6b). Especially the hyperbolic structure of the stagnation type velocity field causes an exponentially fast pinching of the HFT into a thin layer.

To show this behavior more explicitly, we have solved Eq. (12) at  $z = 0$  analytically with the result

$$\bar{x} = \text{arcsinh} [\cosh \bar{x}_0 (\cosh \bar{t} \tanh \bar{x}_0 + \sinh \bar{t} \tanh \bar{y}_0)], \quad (13)$$

$$\bar{y} = \text{arcsinh} [\cosh \bar{y}_0 (\cosh \bar{t} \tanh \bar{y}_0 + \sinh \bar{t} \tanh \bar{x}_0)]. \quad (14)$$

Here we have used

$$\bar{t} = \frac{V_s t}{2 l_{\text{sh}}}, \quad (15)$$

while  $\bar{x} = x/l_{\text{sh}}$ ,  $\bar{x}_0 = x_0/l_{\text{sh}}$  and similarly for the other spatial variables. The lengthy derivation of this solution is omitted here, but it can be verified in a straightforward manner by direct substitution into (12).

Mathematically the obtained deformations (13) and (14) form a one-parameter group of diffeomorphisms, with the parameter  $t$ . So if  $\mathcal{F}_{t_1}$  and  $\mathcal{F}_{t_2}$  are elements of this group corresponding to times  $t_1$  and  $t_2$ , respectively, their composition is  $\mathcal{F}_{t_2} \circ \mathcal{F}_{t_1} = \mathcal{F}_{t_1+t_2}$ . In particular,  $\mathcal{F}_{-t} \circ \mathcal{F}_t = \mathcal{F}_0 \equiv \mathcal{I}d$ , which means that one can reverse the deformations by changing the variables in (13)–(14) as  $\bar{t} \rightarrow -\bar{t}$ ,  $\bar{x} \leftrightarrow \bar{x}_0$  and  $\bar{y} \leftrightarrow \bar{y}_0$  to get

$$\bar{x}_0 = \text{arcsinh} [\cosh \bar{x} (\cosh \bar{t} \tanh \bar{x} -$$

$$\sinh \bar{t} \tanh \bar{y}], \quad (16)$$

$$\bar{y}_0 = \operatorname{arcsinh} [\cosh \bar{y} (\cosh \bar{t} \tanh \bar{y} - \sinh \bar{t} \tanh \bar{x})]. \quad (17)$$

By construction, the velocity field (11) and the corresponding finite deformations (13)–(17) are incompressible. So the plasma elements are distorted by these deformations mainly due to compression in one direction and stretching in the other. We can measure such a distortion by again using the degree of squashing (5) defined earlier, but using Lagrangian mappings (13)–(14) or (16)–(17) instead of the field line mapping. Due to the incompressibility of the Lagrangian deformations, the corresponding degree of squashing  $Q_L$  has simpler form than  $Q$ , given by

$$Q_L = \left( \frac{\partial x_0}{\partial x} \right)^2 + \left( \frac{\partial x_0}{\partial y} \right)^2 + \left( \frac{\partial y_0}{\partial x} \right)^2 + \left( \frac{\partial y_0}{\partial y} \right)^2. \quad (18)$$

A plot of the distribution of  $Q_L$  in the  $(x, y)$ -plane at  $z = 0$  clearly demonstrates that the squashing of plasma elements is concentrated in a layer-like region inclined to the  $x$ -axis by  $45^\circ$  (Figure 7). We define the thickness  $\delta$  and the width  $\Delta$  of this layer as the minimum and maximum extension of the contour  $Q_L(x, y) = Q_{L\max}/2$  in the  $(x, y)$ -plane, respectively. Here

$$Q_{L\max} = 2 + 4 \sinh^2 \bar{t} \quad (19)$$

is the maximum of  $Q_L$  which is located at  $\mathbf{r} = 0$ . For sufficiently large times  $\bar{t} \gtrsim 1$  we obtain

$$\delta \simeq 2\sqrt{2} e^{-\bar{t}} l_{\text{sh}}, \quad (20)$$

$$\Delta \simeq 2.5 l_{\text{sh}}. \quad (21)$$

Thus, under a “twisting” shearing motion applied to the HFT feet a layer-like structure forms in the middle of the HFT. The thickness of this layer decreases exponentially fast in time, while its width remains approximately constant.

As we will show in § 5 this effect is actually enhanced if magnetic forces are taken into account. In many respects this process resembles the pinching of a magnetic rope in laboratory plasmas, which has been realized in 2D theory of current sheets long time ago (Syrovatskii 1981). Our model generalizes this process to 3D and for this reason we gave it the name magnetic pinching.

An important question we have not addressed yet is what impact the pinching has on the current density within the HFT. We start by computing the  $z$ -component of the current density  $\mathbf{j}$  in the midplane  $z = 0$  and the photospheric planes  $z = \pm L$  in our so

far the purely kinematic model of the pinching process. As the velocity field is known the calculation can be carried out using the induction equation and Ampère’s law. The results are shown in Figure 8 for the time  $\bar{t} = 2.5$ . A comparison of Figures 7 and 8b shows that the distributions of  $j_z$  and  $Q_L$  in the plane  $z = 0$  have nearly the same shapes. The  $j_z$  distribution becomes noticeably different from the  $Q_L$  distribution only in the inflow region near the current layer, where spikes of reverse current appear. Such a similarity between the two distributions indicates that in this kinematic picture the current layer forms as a direct consequence of the strong squashing of Lagrangian elements. The presence of the reverse currents in the inflow regions is very interesting as similar features are also found in exact (Sonnerup & Priest 1975; Craig & Henton 1995; Priest et al. 2000) and in numerical (Biskamp 1986) investigations of 2D reconnection. It is a nice surprise to see that these features are reproduced in our 3D kinematic model. The reverse currents do not only exist in the midplane ( $z = 0$ ), but also in the planes  $z = \pm L$  where they have a slightly asymmetric form (Figure 8a, c). The current layer in these planes is mainly produced by the shearing flows along the  $y$ -axis ( $z = L$ ) or the  $x$ -axis ( $z = -L$ ), which are induced by given velocity field. In consequence, the current layer is wider, and longer than in the midplane, and nearly parallel to one of the coordinate axes. Owing to symmetry of the initial configuration and of the applied boundary motions (see Figures 2, 3 and 5) the spatial distribution of  $j_z$  in the planes  $z = L$  and  $z = -L$  is very similar except that for  $z = -L$  the layer is aligned with the  $x$ -axis whereas for  $z = L$  it is aligned with the  $y$ -axis. Thus the orientation of the current layer is twisted by approximately  $90^\circ$  when moving from the lower to the upper boundary plane.

Further interesting properties of the pinching process can be learned from studying the time evolution of the magnetic field and the current density distribution in the plane  $z = 0$  along the line  $y = -x$ . This is most conveniently carried out in a new  $((x', y'))$  coordinate system in which one of the axis ( $x'$ ) is aligned with the current layer. This coordinate system is rotated by  $45^\circ$  with respect to the original one. The detailed derivation of the magnetic field component  $B_{x'}$  is described in Appendix B, while here we only present the resulting expression:

$$B_{x'} = B_{x'1} + B_{x'2}, \quad (22)$$

$$B_{x'1} = -\sqrt{2} h l_{\text{sh}} e^{\bar{t}} \cosh\left(\frac{\bar{y}'}{\sqrt{2}}\right) \frac{\text{arcsinh}\left[e^{\bar{t}} \sinh\left(\frac{\bar{y}'}{\sqrt{2}}\right)\right]}{\left[1 + \left(e^{\bar{t}} \sinh\left(\frac{\bar{y}'}{\sqrt{2}}\right)\right)^2\right]^{1/2}}, \quad (23)$$

$$B_{x'2} = -\frac{B_{\parallel} l_{\text{sh}}}{\sqrt{2} L} \text{cotanh}\left(\frac{\bar{y}'}{\sqrt{2}}\right) \ln\left[\frac{1 + \left(e^{\bar{t}} \sinh\left(\frac{\bar{y}'}{\sqrt{2}}\right)\right)^2}{1 + \sinh^2\left(\frac{\bar{y}'}{\sqrt{2}}\right)}\right]. \quad (24)$$

The  $B_{x'1}$  contribution is caused by the stretching of the transverse magnetic field along the  $x'$ -axis due to the hyperbolic structure of the flow in the middle of the HFT. The  $B_{x'2}$  contribution appears because of the  $B_z$ -component is sheared by a non-vanishing gradient of the flow in the  $z$ -direction. Notice that this second effect, contrary to the first one, is purely three-dimensional.

Despite this difference the spatial and time variation of  $B_{x'1}$  and  $B_{x'2}$  are quite similar. In both cases a steepening of the profiles occurs at  $\bar{y}' = 0$  and the field is piled up at  $\bar{t} \gtrsim 1.5$  close to the steepening fronts (cf. Figures 9a, b). This means that the corresponding profiles of the current densities  $j_{z1} \approx -\frac{\partial B_{x'1}}{\partial y'}$  and  $j_{z2} \approx -\frac{\partial B_{x'2}}{\partial y'}$  have growing and narrowing positive peaks at  $\bar{y}' = 0$  which for  $\bar{t} \gtrsim 1.5$  are enclosed by extended regions of reverse current (Figures 9c, d). With the help of (22)–(24) one can find the maximum current density  $j_z^*$  at  $\bar{t} \gtrsim 1$  given by

$$j_z^* \equiv j_z|_{\mathbf{r}=0} \simeq e^{2\bar{t}} \frac{h}{\mu_0} \left( 1 + \frac{B_{\parallel}}{2hL} \right), \quad (25)$$

which shows that for sufficiently large displacements of the spots the kinematic HFT pinching causes an exponential growth of the current density in the middle of the HFT. An exact form of  $j_z^*$  (see below) contains the factor  $2 \sinh(2\bar{t})$  instead of  $e^{2\bar{t}}$ , which gives the correct linear growth of  $j_z^*$  at  $2\bar{t} \lesssim 1$  as expected.

Appendix B presents the technique which allows the derivation of the  $j_z$ -distribution along the complete quasi-separator. Using this technique we obtain

$$\dot{j}_{z \text{ qs}} = \dot{j}_{z \text{ qs1}} + \dot{j}_{z \text{ qs2}}, \quad (26)$$

$$j_{z \text{ qs1}} = \frac{\sinh(2\bar{t}\sqrt{1-\bar{z}^2})}{\sqrt{1-\bar{z}^2}} \frac{1}{\mu_0} \left( \frac{\partial B_{0x}}{\partial x} - \frac{\partial B_{0y}}{\partial y} \right) \Big|_{\text{qs}}, \quad (27)$$

$$j_{z \text{ qs2}} = \left[ \sinh(2\bar{t}\sqrt{1-\bar{z}^2}) - 2\bar{z}^2\bar{t}\sqrt{1-\bar{z}^2} \right] \frac{B_{0z}|_{\text{qs}}/(\mu_0 L)}{(1-\bar{z}^2)^{3/2}}. \quad (28)$$

Here the index qs means that the corresponding magnitudes are evaluated at  $\mathbf{r} = (0, 0, z)$  resulting in

$$\left( \frac{\partial B_{0x}}{\partial x} - \frac{\partial B_{0y}}{\partial y} \right) \Big|_{\text{qs}} = 6\bar{d}^2\bar{l}^2 \frac{B_s}{L} \left\{ \left[ \bar{l}^2 + (1 + \bar{d} + \bar{z})^2 \right]^{-5/2} + \left[ \bar{l}^2 + (1 + \bar{d} - \bar{z})^2 \right]^{-5/2} \right\}, \quad (29)$$

$$B_{0z}|_{\text{qs}} = 2B_s\bar{d}^2 \left\{ \frac{1 + \bar{d} + \bar{z}}{\left[ \bar{l}^2 + (1 + \bar{d} + \bar{z})^2 \right]^{3/2}} + \right.$$

$$\left. \frac{1 + \bar{d} - \bar{z}}{[\bar{t}^2 + (1 + \bar{d} - \bar{z})^2]^{3/2}} \right\}. \quad (30)$$

In the derivation of (26)–(28) we also used that  $\frac{\partial B_{0y}}{\partial x}\Big|_{\text{qs}} = \frac{\partial B_{0x}}{\partial y}\Big|_{\text{qs}} \equiv 0$  for our configuration (1).

Putting  $\bar{z} \rightarrow \mp 1$  in (26)–(28), one obtains  $j_z$  at the footpoints of the quasi-separator

$$j_{z \text{ qsf}} = \frac{2\bar{t}}{\mu_0} \left( \frac{\partial B_{0x}}{\partial x} - \frac{\partial B_{0y}}{\partial y} + \frac{B_{0z}}{L} \right) \Big|_{\text{qsf}} + \frac{4\bar{t}^3}{3\mu_0 L} B_{0z} \Big|_{\text{qsf}}, \quad (31)$$

where the index qsf denotes the evaluation of the corresponding magnitudes at  $\mathbf{r} = (0, 0, \mp L)$ . Thus, the current density at the feet of the HFT grows only with the third power of time, which is much slower than the exponential growth in the middle of the HFT. This difference is due to the fact that motions at the HFT feet (8)–(9) just shear the magnetic field. Such a pure shearing motion is less effective in generating current than the “hyperbolic superposition” in the middle of the HFT.

However, the local gradients of magnetic field are much larger at the feet than in the middle, therefore the maxima of  $j_{z \text{ qs1}}$  remain located at the feet even for the times during which the sunspots have moved over distances comparable with  $L$  (Figure 10a). By contrast, the second contribution to the current density ( $j_{z \text{ qs2}}$ ) has a maximum in the middle of the HFT at comparable times (Figure 10b) because of the above mentioned exponential growth and a relatively small gradient of  $B_{0z}$  along the quasi-separator.

## 5. FORCE-FREE PINCHING OF THE HFT

In the kinematic model of the HFT pinching process we considered so far, the force balance is taken into account only qualitatively by constructing deformations of the HFT which are in agreement with its elastic properties. However, the layer-like structure obtained in the kinematic model for the middle part of the HFT enables us to improve the model by determining the distributions of the field and current density across such a layer for a force-free evolution of the configuration.

Indeed, at each time such a force-free evolution can be represented as a deformation of the initial potential field obeying the frozen-in condition. One can always decompose such a deformation into the kinematic “pinching” deformation considered so far and an additional “relaxing” deformation in which the configuration settles into a force-free state. As shown above, after the pinching deformation unbalanced magnetic stresses accumulate in

the middle of the HFT, mainly in a thin layer parallel to the plane  $y' = 0$ . This is due to an increase of the  $B_{x'}$ -component and the magnetic pressure it causes near this plane, so that the corresponding unbalanced force is directed towards the plane acting as if to compress the layer. We conclude that the relaxing deformation will compress the middle part of the HFT. The layer-like distribution of the unbalanced stresses implies that this compression will be essentially one-dimensional. Since  $B_z$ , unlike  $B_{x'}$ , does not vanish inside the layer, the corresponding compression is indeed able to provide the required balance of magnetic forces inside the layer. With the expressions (22)–(24) for  $B_{x'}$  and taking  $B_{\parallel}$  for  $B_z$  as initial values, one can use the frozen-in condition (see (B2)) to obtain the components of the equilibrium field as

$$B_{x' \text{ eq}} \simeq B_{x'}|_{\bar{y}'=\bar{y}'_0} \left( \frac{\partial \bar{y}'}{\partial \bar{y}'_0} \right)^{-1}, \quad (32)$$

$$B_{z \text{ eq}} \simeq B_{\parallel} \left( \frac{\partial \bar{y}'}{\partial \bar{y}'_0} \right)^{-1}. \quad (33)$$

These magnetic field components have to satisfy the force-free condition

$$B_{x' \text{ eq}}^2 + B_{z \text{ eq}}^2 \simeq \text{const}, \quad (34)$$

which together with (32) and (33) yields the equation for determining the relaxing deformation  $\bar{y}'(\bar{y}'_0)$  or, in other words, the relationship between Eulerian ( $\bar{y}'$ ) and Lagrangian coordinates ( $\bar{y}'_0$ ). The constant in (34) is naturally fixed by the condition that  $\partial \bar{y}' / \partial \bar{y}'_0 = 1$  at the point  $\bar{y}'_0 = \bar{y}'_{0m}$ , where the initial current density and the unbalanced Lorentz force vanish and so the relaxing deformation should have no effect on the neighborhood of this location. Therefore, at this point  $\partial B_{x'} / \partial \bar{y}'_0 \approx 0$  and  $B_{x'}$  reaches a local maximum  $B_{x'm}^2$ . This makes it possible to derive from (32)–(34) the required equation

$$\frac{\partial \bar{y}'}{\partial \bar{y}'_0} = \left( \frac{1 + B_{x'}^2|_{\bar{y}'=s} / B_{\parallel}^2}{1 + B_{x'm}^2 / B_{\parallel}^2} \right)^{1/2}, \quad (35)$$

where  $B_{x'm}^2$  depends on time and the parameters of the model as shown below. At a fixed time this is an ordinary differential equation for  $\bar{y}'(\bar{y}'_0)$ , which can be immediately integrated to give

$$\bar{y}' = \int_0^{\bar{y}'_0} \left( \frac{1 + B_{x'}^2|_{\bar{y}'=s} / B_{\parallel}^2}{1 + B_{x'm}^2 / B_{\parallel}^2} \right)^{1/2} ds. \quad (36)$$

By differentiating (32) and (35) (to obtain an expression for  $\partial^2 \bar{y}' / \partial \bar{y}'_0{}^2$ ) one can also derive the equilibrium current density,

$$j_{z \text{ eq}} \simeq -\frac{1}{\mu_0 l_{\text{sh}}} \frac{\partial B_{x'}}{\partial \bar{y}'} \Big|_{\bar{y}'=\bar{y}'_0} \frac{1 + B_{x'm}^2 / B_{\parallel}^2}{\left( 1 + B_{x'}^2|_{\bar{y}'=\bar{y}'_0} / B_{\parallel}^2 \right)^2}. \quad (37)$$

Thus, Eqs. (32), (33) and (35)–(37) determine the distributions of the equilibrium magnetic field and current density across the current layer in the middle of the HFT in parametric form with  $\bar{y}'_0$  as a parameter. Examples of the  $B_{x' \text{ eq}}$ - and  $B_{z \text{ eq}}$ -profiles at different times are shown in Figure 11. The plots show that the steepening of  $B_{x' \text{ eq}}$  in time is accompanied by a corresponding compression of  $B_{z \text{ eq}}$  inside the current layer.

For the especially interesting large time regime ( $\bar{t} \gtrsim 1$ ) one can show that two extrema of  $B_{x'}$  are located at

$$\bar{y}'_{0\text{m}} \simeq \pm \frac{\delta}{2l_{\text{sh}}} F \left( \frac{B_{\parallel}}{hL} \right). \quad (38)$$

In this expression  $F$  is a relatively complicated function of its argument which we do not write down explicitly here, but it turns out that  $F$  only increases from 1.51 to 1.98 when its argument  $B_{\parallel}/hL$  varies from 0 to infinity, so that to a good approximation (38) is given by

$$\bar{y}'_{0\text{m}} \simeq \delta/l_{\text{sh}}. \quad (39)$$

So an estimate of  $B_{x' \text{ m}}$  can be obtained by evaluating (22) at  $\bar{y}' = \bar{y}'_{0\text{m}}$  under the assumption  $\bar{t} \gtrsim 1$  with the result

$$\frac{B_{x' \text{ m}}^2}{B_{\parallel}^2} \simeq e^{2\bar{t}} \left( 0.91 \frac{hl_{\text{sh}}}{B_{\parallel}} + 0.57 \frac{l_{\text{sh}}}{L} \right)^2. \quad (40)$$

Substitution of this value and  $B_{x'}|_{\bar{y}'=0} = 0$  into (37) enables us to express the equilibrium current density at  $\mathbf{r} = 0$  in terms of the corresponding parameters of the initial configuration,

$$j_{z \text{ eq}}^* \simeq e^{2\bar{t}} \frac{h}{\mu_0} \left( 1 + \frac{B_{\parallel}}{2hL} \right) \left[ 1 + e^{2\bar{t}} \left( 0.91 \frac{hl_{\text{sh}}}{B_{\parallel}} + 0.57 \frac{l_{\text{sh}}}{L} \right)^2 \right]. \quad (41)$$

It follows that the “relaxing” compression gives rise to an additional term in the force-free current density in comparison with its kinematic analogue (25). This term grows exponentially in time and increases with decreasing  $B_{\parallel}$ . In particular, in the limit  $B_{\parallel} \rightarrow 0$  we would formally obtain that  $|j_{z \text{ eq}}^*| \rightarrow \infty$ , which is in good agreement with the results for current accumulation at a null point (Bulanov & Olshanetsky 1984; Priest & Titov 1996; Rickard & Titov 1996).

## 6. IMPLICATIONS FOR SOLAR FLARES

Figure 12 shows the dependence of the current density (41) on the geometrical parameters  $l/L$  and  $d/L$  of our “straightened” HFT for the time  $\bar{t} = 2.5$ , where  $h$ ,  $B_{\parallel}$  and  $l_{\text{sh}}$  are



given by (3), (4) and (10), respectively. The largest values of  $j_{z\text{ eq}}^*$  at this time are reached if  $l/L \rightarrow 1$  and  $d/L \approx 0.5$  and they can exceed the characteristic current density  $B_s/(\mu_0 L)$  in the configuration by more than a factor  $10^3$ . Higher values of  $j_{z\text{ eq}}^*$  can formally be reached at larger  $\bar{t}$  but they do not seem to be realistic, because it is more likely that the current layer will be disrupted by the onset of the tearing instability before that.

We evaluate the characteristics of the pinched HFT at the time  $\bar{t} = 2.5$  for the same parameters ( $l/L = 0.5$  and  $d/L = 0.4$ ) as used in Figure 2. Assume that  $L = 50$  Mm and  $B_s = 800$  G, then for our “straightened” model HFT we obtain that the transverse and longitudinal fields near the current layer are  $B_{x'm} \simeq 470$  G and  $B_{\parallel} \simeq 218$  G, respectively. Inside the layer  $B_z|_{r=0} \simeq 518$  G due to the compression of the longitudinal field by relaxation, so that the corresponding compression factor is about 2.8.

To get a rough estimate of the free magnetic energy associated with the current layer, one can use the 2D solution found by Syrovatskii (1981) as an approximation, because the current density in our model is mainly concentrated in a thin layer of width  $\Delta$  and length  $2L$ . Then in our notation the total current in the layer is

$$I \simeq \frac{\pi}{2\mu_0} B_{x'm} \Delta, \quad (42)$$

while the magnetic flux associated with the current is given by

$$\mathcal{L}I \simeq \frac{1}{4} \left( 1 + \ln \frac{8L}{\Delta} \right) B_{x'm} \Delta, \quad (43)$$

where  $\mathcal{L}$  is the inductance of the current sheet per unit length. The corresponding magnetic energy is

$$W \simeq \mathcal{L}I^2 L \simeq \frac{\pi}{8\mu_0} \left( 1 + \ln \frac{8L}{\Delta} \right) B_{x'm}^2 \Delta^2 L, \quad (44)$$

which for the parameter values given above yields  $W \simeq 1.3 \times 10^{26}$  J. This amount of energy is even more than needed to produce a large flare and it is build up in our model over a reasonable time period of  $t = 2.5 \times 2l_{\text{sh}}/V_s \simeq 3.6$  h, if a sunspot velocity  $V_s = 5$  km s<sup>-1</sup> is assumed.

For the same parameter values the maximum current density is given by  $j_{z\text{ eq}}^* \simeq 0.33$  Am<sup>-2</sup>, which is not large enough for the Spitzer resistivity to be important. Indeed, the local magnetic Reynolds number for our current layer is

$$Re_m = \frac{V_s B_s}{\eta j_{z\text{ eq}}^*} \simeq 44 \gg 1, \quad (45)$$

where the same sunspot velocity as above has been assumed and the Spitzer resistivity  $\eta$  is evaluated at the coronal temperature  $T = 2 \times 10^6$  K.

The current density in such a layer is also not large enough for the onset of the ion-acoustic instability, since the corresponding critical current density  $j_{\text{is}} = enc_{\text{is}} \simeq 49 \text{ A m}^{-2}$  is much larger than  $j_{z\text{eq}}^*$ . In this estimate of  $j_{\text{is}}$  the evaluated compression factor is taken into account, so that the plasma density inside the sheet is taken to be  $n = 2.8 \times 10^{15} \text{ m}^{-3}$ . The sound speed  $c_{\text{is}} = (k_{\text{B}}T/m_{\text{p}})^{1/2}$  is estimated for the coronal temperature given above. Other micro-instabilities are characterized by similar or even larger critical values of the current density (Somov 1992; Priest & Forbes 2000) so that their development in our current layer is also hardly possible.

For the tearing instability the present state of the theory, based on rather idealized models, does not allow us to draw any reliable conclusions about its possible onset in the layer. Intuitively, however, this seems to be quite a plausible possibility and has some support from 2.5D numerical simulations of current layer formation in quadrupole configurations (Hirose et al. 2001). We believe that our 3D configuration therefore deserves careful studies regarding this aspect in the future. We will here assume that the current layer generated by the HFT pinching process is unstable to the tearing mode as a working hypothesis to see how this assumption fits in with other known facts about flares.

In this sense we can say that the current layer in a pinched HFT will be more unstable the larger the value of the current density  $j_{z\text{eq}}^*$  is for given sunspot displacements. As mentioned above,  $j_{z\text{eq}}^*$  grows very fast with decreasing  $B_{\parallel}$ , which means that HFTs with smaller initial values of  $B_{\parallel}$  will be more unstable. This fits in very well with the existence of two observationally different classes of flares, the so-called less-impulsive and more-impulsive flares (Sakao et al. 1998). Such a distinct difference between the flares could be due to the strong dependence of  $j_{z\text{eq}}^*$  on  $B_{\parallel}$  found above. A similar explanation has previously been proposed qualitatively by Somov & Kosugi (1997).

We have demonstrated above that a “twisting” shearing motion at the HFT feet leads to the pinching of its middle parts into a thin current layer with a free magnetic energy sufficient for a large solar flare. This kind of photospheric motion is in a good agreement with the observational fact that large flares occur frequently in the configurations with an S-shaped photospheric polarity inversion line (Martres et al. 1966; Moreton & Severny 1968). Such a relationship has been demonstrated first by Gorbachev & Somov (1988) in a potential field model of a quadrupole configuration using monopole sources. These results have been confirmed and quantified generalizing the separator field line, on which Gorbachev & Somov (1988) have based their analysis, to an HFT.

Another remarkable feature of the HFT pinching process considered in this paper is the increase of the plasma density inside the current layer due to the compression of the longitudinal field by relaxation under the frozen-in condition. As can be seen from our estimates, this relaxation leads to a compression of the coronal plasma inside the layer by up to one order of magnitude, which may be sufficient for the onset of thermal instability and, hence, for an additional condensation of plasma in the current layer. Such a side effect of the pinching process has two important implications.

First, the accumulation of plasma inside the current layer in the pre-flare state increases the number of electrons available for acceleration in the subsequent impulsive phase of the flare when the layer becomes unstable. This can help to solve the electron number problem of particle acceleration in flares (Miller et al. 1997). The observational evidence recently reported by Kliem et al. (2002) provides support for this point of view.

Secondly, the compression and condensation of plasma in the pinching HFT is a good candidate for a 3D mechanism of prominence formation in the solar corona under suitable physical conditions. At present such a mechanism has only been investigated in the framework of a 2.5D numerical model (Hirose et al. 2001). Its generalization to the 3D geometry of the HFT might help to develop a unified theory of solar flares and prominence formation, two phenomena which so far seemed to be completely unrelated.

## 7. CONCLUSIONS

We have found that the fundamental condition for the formation of layers of particularly strong current density (pinching) inside hyperbolic flux tubes (HFTs) are photospheric shearing motions which twist the HFT around its axis. Photospheric motions which merely turn the HFT have a much weaker effect. We plan to study in more detail in the following papers of this series how combinations of these two extreme types of photospheric motions influence the HFT pinching. Also the obtained results must be valid for configurations with separator field lines and their associated separatrix surfaces, since such structures are a limiting case of HFTs.

Due to the special elastic properties of the HFT the photospheric shearing motions easily propagate into the corona and meet each other in the middle of the HFT. If the shearing motions are applied to the HFT feet in a way as if trying to cause a torsion of the HFT, their superposition in the middle of the HFT forms a hyperbolic flow pattern which is inclined by  $45^\circ$  with respect to the hyperbolic structure of the transverse magnetic field inside the HFT. Such an arrangement of the transverse velocity and magnetic fields

provides an exponentially growing current density ordered in a layer-like structure along the HFT. The width of the current layer is of the order of the characteristic size of the shearing motions, while its thickness decreases exponentially fast in time.

There are basically two physical effects which are responsible for the process of HFT pinching. First, the hyperbolic component of the flow is incompressible and so does not change the longitudinal magnetic field in the HFT. However, it causes a large squashing of plasma elements along the forming layer and this squashing increases the transverse magnetic field near the layer enormously in comparison with the initial state. Therefore, the strength of the resulting transverse field can easily approach that of the longitudinal field and even exceed it, depending on the initial conditions and the duration of the flow. The increase of the transverse field causes a second effect – the compression of the longitudinal field and plasma across the layer, which leads to an additional increase of the current density inside the layer.

The exponential time dependence of the basic physical quantities inside the current layer can also be translated into a similar dependence on sunspot displacements. For a quadrupole configuration with an HFT we can estimate that the displacements of the spots over distances comparable with the distances between them are sufficient to build up magnetic energy inside the pinched HFT as is required for a large solar flare. The large current density and gradient of magnetic shear inside the layer provide favorable conditions for the onset of the tearing instability in the layer and its transition to a turbulent state with a large rate of reconnection and magnetic energy release.

The authors are grateful to the anonymous referee for a number of useful comments. VT thankfully acknowledges financial support from the Volkswagen-Foundation. KG and TN thank the UK’s Particle Physics and Astronomy Research Council for support through Advanced Fellowships. This work has been supported in part by the European Community’s Human Potential Programme under contract HPRN-CT-2000-00153, PLATON.

## A. JACOBIAN MATRIX OF THE FIELD LINE MAPPING

For an analytical investigation of the field line mapping in a given magnetic configuration it is useful to have a method for calculating the Jacobian matrix of this mapping. Below such a method is developed and applied to calculate the squashing degree at the quasi-separator of the “straightened” HFT (see § 3).

Let  $\mathbf{B}(\mathbf{r})$  define a magnetic field and

$$\mathbf{R}(\tau, \mathbf{r}_+) \equiv (X(\tau, \mathbf{r}_+), Y(\tau, \mathbf{r}_+), Z(\tau, \mathbf{r}_+))$$

represent its field lines starting at points  $\mathbf{r}_+ = (x_+, y_+)$  of the positive photospheric polarity located in the plane  $z = z_+$ . The field lines are parameterized by a parameter  $\tau$  such that the corresponding field line equation is

$$\frac{d\mathbf{R}}{d\tau} = \mathbf{B}(\mathbf{R}). \quad (\text{A1})$$

The differentiation of (A1) with respect to  $\mathbf{r}_+$  yields

$$\frac{d\mathcal{D}}{d\tau} = \mathcal{G}\mathcal{D}, \quad (\text{A2})$$

where  $\mathcal{G} \equiv \nabla_{\mathbf{R}}\mathbf{B}$  is the matrix of derivatives of the magnetic field with respect to  $\mathbf{R} = \mathbf{R}(\tau, \mathbf{r}_+)$ , and

$$\mathcal{D} \equiv \mathcal{D}(\tau, \mathbf{r}_+) = \nabla_{\mathbf{r}_+}\mathbf{R}(\tau, \mathbf{r}_+) \equiv \begin{pmatrix} \frac{\partial X}{\partial x_+} & \frac{\partial X}{\partial y_+} \\ \frac{\partial Y}{\partial x_+} & \frac{\partial Y}{\partial y_+} \\ \frac{\partial Z}{\partial x_+} & \frac{\partial Z}{\partial y_+} \end{pmatrix} \quad (\text{A3})$$

is the Jacobian matrix. With its help a variation  $\delta\mathbf{R}$  of the field line point  $\mathbf{R} = \mathbf{R}(\tau, \mathbf{r}_+)$  due to an infinitesimal change  $\delta\mathbf{r}_+ = (\delta x_+, \delta y_+)$  of the corresponding footpoint  $\mathbf{R}_+ = \mathbf{R}(0, \mathbf{r}_+) \equiv (x_+, y_+, z_+)$  is determined by

$$\delta\mathbf{R} = \mathcal{D} \delta\mathbf{r}_+. \quad (\text{A4})$$

The system of nine ordinary differential Eqs. (A1)–(A2) together with the initial conditions

$$\mathbf{R}(0, \mathbf{r}_+) = (x_+, y_+, z_+), \quad (\text{A5})$$

$$\mathcal{D}(0, \mathbf{r}_+) = \begin{pmatrix} 1 & 0 \\ 0 & 1 \\ 0 & 0 \end{pmatrix} \quad (\text{A6})$$

determines the matrix  $\mathcal{D}$  along the field line starting at a point  $\mathbf{r}_+$  on the photosphere. Thus the matrix  $\mathcal{D}$  can be obtained as the result of solving the Cauchy problem defined by Eqs. (A1)–(A2) and (A5)–(A6).

It should be emphasized that the vector  $\delta\mathbf{r}_+$  in Eq. (A4) is two-dimensional, while the vector  $\delta\mathbf{R}$  is three-dimensional. Also for  $\tau = \tau_-$ , corresponding to the footpoint of the

field line on the negative polarity side, i.e. when  $Z(\tau_-, \mathbf{r}_+) = z_-$ , the vector  $\delta\mathbf{R} = \delta\mathbf{R}_-$  is generally not tangent to the photospheric plane. Therefore, to find the photospheric displacement  $\delta\mathbf{r}_-$  corresponding to the negative polarity it is necessary to project  $\delta\mathbf{R}_-$  along the local direction of magnetic field  $\mathbf{B}_- \equiv \mathbf{B}(x_-, y_-, z_-)$  onto the photospheric plane at the footpoint  $(x_-, y_-, z_-) = \mathbf{R}(\tau_-, \mathbf{r}_+)$ . This yields  $\delta\mathbf{r}_- = \mathcal{P} \delta\mathbf{R}_-$ , where

$$\mathcal{P} = \begin{pmatrix} 1 & 0 & -\frac{B_{x-}}{B_{z-}} \\ 0 & 1 & -\frac{B_{y-}}{B_{z-}} \end{pmatrix} \quad (\text{A7})$$

is the projection matrix. Applying the projection matrix to Eq. (A4) and denoting  $\mathcal{D}(\tau_-, \mathbf{r}_+)$  as  $\mathcal{D}_-$ , we get  $\delta\mathbf{r}_- = \mathcal{P}\mathcal{D}_- \delta\mathbf{r}_+$ , which in turn implies that the required matrix is

$$\mathcal{D} \equiv \begin{pmatrix} \frac{\partial X_-}{\partial x_+} & \frac{\partial X_-}{\partial y_+} \\ \frac{\partial Y_-}{\partial x_+} & \frac{\partial Y_-}{\partial y_+} \end{pmatrix} = \mathcal{P}\mathcal{D}_-. \quad (\text{A8})$$

Using this expression for  $\mathcal{D}$  one can find all the characteristics of the field line connectivity we need and, in particular, the squashing degree (5).

We now apply this theory to the calculation of the squashing degree  $Q$  on the quasi-separator of the “straightened” HFT. As already mentioned in § 3, the quasi-separator coincides with the  $z$ -axis in this case. The matrix of magnetic field derivatives on this axis can be reduced to the form

$$\mathcal{G}(0, 0, z) = \begin{pmatrix} f(z) & 0 & 0 \\ 0 & -f(-z) & 0 \\ 0 & 0 & -f(z) + f(-z) \end{pmatrix}, \quad (\text{A9})$$

due to a symmetry of the field (1). Here we have used the definition

$$f(z) = \left. \frac{\partial B_{0x}}{\partial x} \right|_{\mathbf{r}=(0,0,z)}. \quad (\text{A10})$$

In our case it is more convenient to determine the matrix  $\mathcal{D}_-$  by using the coordinate  $z$  rather than the parameter  $\tau$  in (A2). This simply means that instead of  $d\tau$  we have to use  $dz/B_{0z}$  in (A2). The diagonal form of  $\mathcal{G}$  on the quasi-separator then enables us to find  $\mathcal{D}_-$  by integration of (A9) over  $z$ . This and (A7)–(A8), where  $B_{x-} \equiv B_x(0, 0, -L) = 0$  and  $B_{y-} \equiv B_y(0, 0, L) = 0$  are used, after some transformations result in

$$\mathcal{D}_{\text{qs}} \equiv \mathcal{D}|_{\mathbf{r}_+=0} = \begin{pmatrix} e^\lambda & 0 \\ 0 & e^{-\lambda} \end{pmatrix}, \quad (\text{A11})$$

where  $\lambda$  is given by Eq. (7). Then by using the definitions of  $Q$  and  $\mathcal{D}$  (see (5) and (A8)) we obtain the required expression (6).

## B. CONVECTION OF MAGNETIC FIELD BY HYPERBOLIC FLOWS

For a given flow  $\mathbf{r}(t, \mathbf{r}_0)$ , which is related to the velocity field  $\mathbf{v}(t, \mathbf{r})$  by Eq. (12), the general solution of the ideal induction equation

$$\frac{\partial \mathbf{B}}{\partial t} + \nabla \times (\mathbf{B} \times \mathbf{v}) = \mathbf{0} \quad (\text{B1})$$

can be written in the Lagrangian representation as

$$\mathbf{B}(t, \mathbf{r}_0) = \mathbf{B}_0(\mathbf{r}_0) \cdot \nabla_{\mathbf{r}_0} \mathbf{r} / \det(\nabla_{\mathbf{r}_0} \mathbf{r}). \quad (\text{B2})$$

For our purposes, however, the Eulerian representation is more convenient. One can switch to this representation by substituting  $\mathbf{r}_0 \rightarrow \mathbf{r}_0(t, \mathbf{r})$  and  $\nabla_{\mathbf{r}_0} \mathbf{r} \rightarrow (\nabla_{\mathbf{r}} \mathbf{r}_0)^{-1}$  into (B2). Then after some transformations, using the incompressibility condition  $\det(\nabla_{\mathbf{r}_0} \mathbf{r}) = 1$  for the flow (11), we obtain

$$B_x = B_{0x} \frac{\partial \bar{y}_0}{\partial \bar{y}} - B_{0y} \frac{\partial \bar{x}_0}{\partial \bar{y}} + B_{0z} \frac{l_{\text{sh}}}{L} \left( \frac{\partial \bar{x}_0}{\partial \bar{y}} \frac{\partial \bar{y}_0}{\partial \bar{z}} - \frac{\partial \bar{y}_0}{\partial \bar{y}} \frac{\partial \bar{x}_0}{\partial \bar{z}} \right), \quad (\text{B3})$$

$$B_y = B_{0y} \frac{\partial \bar{x}_0}{\partial \bar{x}} - B_{0x} \frac{\partial \bar{y}_0}{\partial \bar{x}} + B_{0z} \frac{l_{\text{sh}}}{L} \left( \frac{\partial \bar{y}_0}{\partial \bar{x}} \frac{\partial \bar{x}_0}{\partial \bar{z}} - \frac{\partial \bar{x}_0}{\partial \bar{x}} \frac{\partial \bar{y}_0}{\partial \bar{z}} \right), \quad (\text{B4})$$

$$B_z = B_{0z}, \quad (\text{B5})$$

where  $\bar{z} = z/L$ , while the  $x, y$ -coordinates are normalized by  $l_{\text{sh}}$ . Thus, the magnetic component  $B_z$  is simply transported by the flow as  $B_z(t, \mathbf{r}) = B_{0z}(\mathbf{r}_0(t, \mathbf{r}))$ . Since the initial component  $B_{0z}(\mathbf{r}_0)$  is almost homogeneous in the middle of the HFT,  $B_z(t, \mathbf{r})$  will remain nearly constant there for a sufficiently long time.

On the other hand, the components  $B_x$  and  $B_y$  will change significantly due to the large gradients of the Lagrangian coordinates. In the plane  $z = 0$  the corresponding derivatives with respect to  $\bar{x}$  and  $\bar{y}$  can be found directly from (16) and (17). The calculation of the derivatives with respect to  $z$  is a less trivial problem and will be considered below.

From the group properties of the flow (see § 4) it follows that the mapping  $\mathbf{r}_0(t, \mathbf{r})$  is described by

$$\frac{d\mathbf{r}_0}{dt} = -\mathbf{v}(\mathbf{r}_0), \quad (\text{B6})$$

where the dependence on  $\mathbf{r}$  is parametric and due to the initial condition  $\mathbf{r}_0(0, \mathbf{r}) = \mathbf{r}$ . Since  $v_z \equiv 0$  the plasma motion is planar such that  $z_0(t, \mathbf{r}) \equiv z$ . Expressions for the other Lagrangian coordinates can be derived explicitly from (B6) and (11) only in the plane  $z = 0$

and only in the case of “twisting” shearing motions, giving (16)–(17). Differentiating (B6) with respect to  $z$  and restricting the result for this plane, one obtains

$$\frac{d}{dt} \frac{\partial \bar{x}_0}{\partial \bar{z}} = -\frac{1}{(\cosh \bar{y}_0)^2} \frac{\partial \bar{y}_0}{\partial \bar{z}} + \tanh \bar{y}_0, \quad (\text{B7})$$

$$\frac{d}{dt} \frac{\partial \bar{y}_0}{\partial \bar{z}} = -\frac{1}{(\cosh \bar{x}_0)^2} \frac{\partial \bar{x}_0}{\partial \bar{z}} - \tanh \bar{x}_0, \quad (\text{B8})$$

which is a system of ordinary differential equations whose unknowns must satisfy the initial conditions

$$\frac{\partial \bar{x}_0}{\partial \bar{z}} = \frac{\partial \bar{y}_0}{\partial \bar{z}} = 0. \quad (\text{B9})$$

In combination with (16)–(17) this system of differential equations allows us to calculate the magnetic components (B3) and (B4) in the plane  $z = 0$  at any time.

Due to a symmetry of the flow, we can make further analytical progress for the particular streamline  $\bar{y} = -\bar{x}$  in the plane  $z = 0$ . The system of differential equations can in this case be integrated explicitly to yield

$$\frac{\partial \bar{x}_0}{\partial \bar{z}} = \frac{\partial \bar{y}_0}{\partial \bar{z}} = \frac{[1 + (e^{\bar{t}} \sinh \bar{y})^2]^{1/2}}{2e^{\bar{t}} \sinh \bar{y}} \ln \left( \frac{1 + (e^{\bar{t}} \sinh \bar{y})^2}{1 + \sinh^2 \bar{y}} \right), \quad (\text{B10})$$

which enables us to find  $B_x$  and  $B_y$  according to the algorithm described above. Using the simplified form of magnetic field (2) and the system of  $(x', y')$ -coordinates rotated by  $45^\circ$  with respect to  $x$  and  $y$ , one obtains the required field component (22). The current density along the quasi-separator (26)–(28) is found in a similar way.

## REFERENCES

- Aly, J. J., & Amari, T. 1989, *A&A*, 221, 287
- Biskamp, D. 1986, *Phys. Fluids*, 29, 1520
- Bulanov, S. V., & Olshanetsky, M. A. 1984, *Phys. Lett.*, 100A, 35
- Cowley, S. C., Longcope, D. W., & Sudan, R. N. 1997, *Phys. Rep.*, 283, 227
- Craig, I. J. D., & Henton, S. M. 1995, *ApJ*, 450, 280
- Démoulin, P., Bagalá, L. G., Mandrini, C. H., Hénoux, J. C., & Rovira, M. G. 1997, *A&A*, 325, 305



- Galsgaard, K. 2000, *J. Geophys. Res.*, 105, 5119
- Galsgaard, K., & Nordlund, Å. 1996, *J. Geophys. Res.*, 101, 13445
- Gorbachev, V. S., & Somov, B. V. 1988, *Sol. Phys.*, 117, 77
- Hirose, S., Uchida, Y., Uemura, S., & Yamaguchi, T. 2001, *ApJ*, 551, 586
- Inverarity, G. W., & Titov, V. S. 1997, *J. Geophys. Res.*, 102, 22285.
- Lau, Y.-T., & Finn, J. M. 1990, *ApJ*, 350, 672
- Longcope, D. 2002, *Phys. Plasmas*, 8, 5277
- Longcope, D. W., & Strauss, H. R. 1994, *ApJ*, 437, 851
- Low, B. C., 1987, *ApJ*, 323, 358
- Kliem, B., Dammasch, E., Curdt, W., & Wilhelm, K. 2002, *ApJ*, 568, L61.
- Martres, M.-J., Michard, R., & Soru-Escout, I. 1966, *Ann. Astrophys.*, 29, 249
- Miller, J. A., et al. 1997, *J. Geophys. Res.*, 102, 14631
- Moreton, G. E., & Severny, A. B. 1968, *Sol. Phys.*, 3, 282
- Parker, E. N. 1972, *ApJ*, 174, 499
- Parker, E. N. 1994, *Spontaneous Current Sheets in Magnetic fields: with Applications to Stellar X-rays* (New York: Oxford University Press)
- Priest, E. R., & Démoulin, P. 1995, *J. Geophys. Res.*, 100, 23443
- Priest, E. R., & Forbes, T. G. 2000, *Magnetic Reconnection: MHD Theory and Applications* (Cambridge: Cambridge University Press)
- Priest, E. R., & Titov, V. S. 1996, *Philos. Trans. R. Soc. London A*, 354, 2951
- Priest, E. R., Titov, V. S., Grundy, R. E., & Hood, A. W. 2000, *Proc. Roy. Soc. Lond. A*, 456, 1821
- Rickard, G. J., & Titov, V. S. 1996, *ApJ*, 472, 840
- Sakao, T., Kosugi, T., & Masuda, S. 1998, in *Observational Plasma Astrophysics: Five Years of Yohkoh and Beyond*, eds. T. Watanabe, T. Kosugi, & A. C. Sterling (Dordrecht: Kluwer), 273

- Somov, B. V. 1992, *Physical Processes in Solar Flares* (Dordrecht: Kluwer)
- Somov, B. V., & Kosugi, T. 1997, *ApJ*, 485, 859
- Sonnerup, B. U. Ö., & Priest, E. R. 1975, *J. Plasma Phys.*, 14, 283
- Seehafer, N. 1986, *Sol. Phys.*, 105, 223
- Syrovatskii, S. I. 1981, *ARA&A*, 19, 163
- Sweet, P. A. 1969, *ARA&A*, 7, 149
- Titov, V. S., & Hornig, G. 2002, *Adv. Space Res.*, 29, 1087
- Titov, V. S., Priest, E. R., & Démoulin, P. 1993, *A&A*, 276, 564
- Titov, V. S., Démoulin, P., & Hornig, G. 1999, in *Magnetic Fields and Solar Processes*, ed. A. Wilson, (Noordwijk: Eur. Space Agency Spec. Publ.), 715
- Titov, V. S., Hornig, G., & Démoulin, P. 2002, *J. Geophys. Res.*, 107, A8, doi:10.1029/2001JA000278.
- Vekstein, G. E., Priest, E. R., & Amari, T. 1991, *A&A*, 243, 492

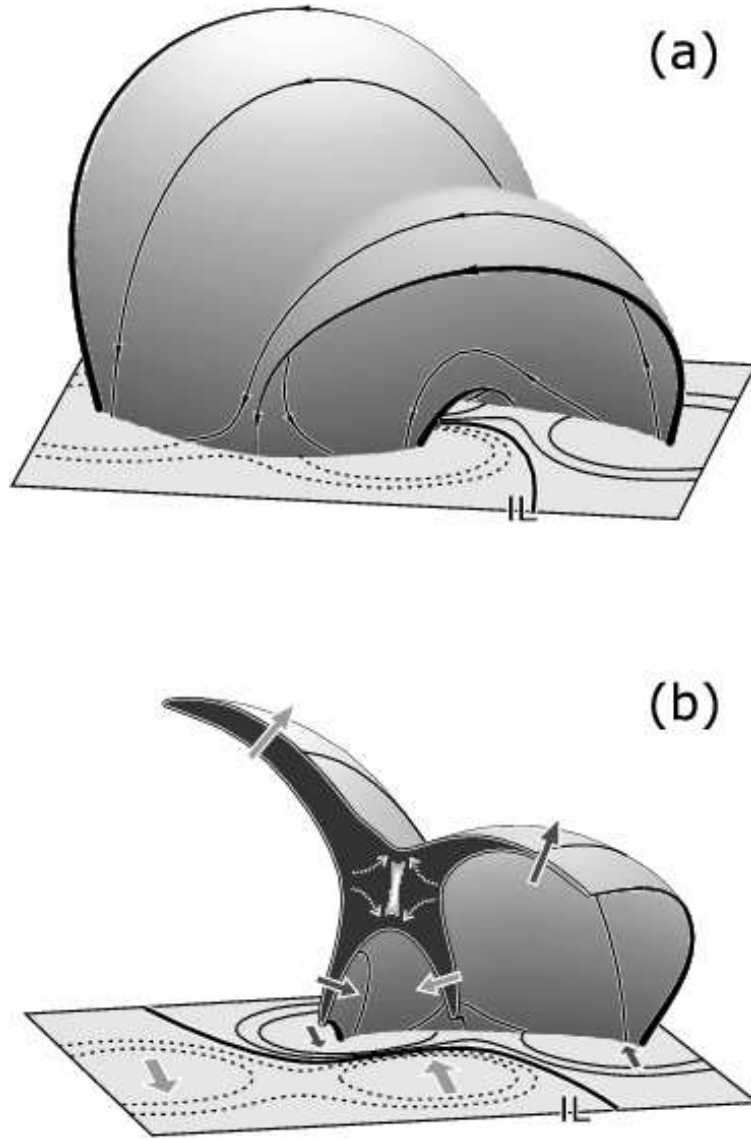


Fig. 1.— Hyperbolic flux tube (a) and half of it (b) in a quadrupole configuration. The varying thickness of the field lines at the “ribs” of the HFT depicts the corresponding variation of the field strength or their “rigidity”. The large arrows on (b) show the directions of plasma flows which lead to the current layer formation in the middle of the HFT. The flows in the corona are due to the appropriate sunspot motions and elastic properties of the HFT.

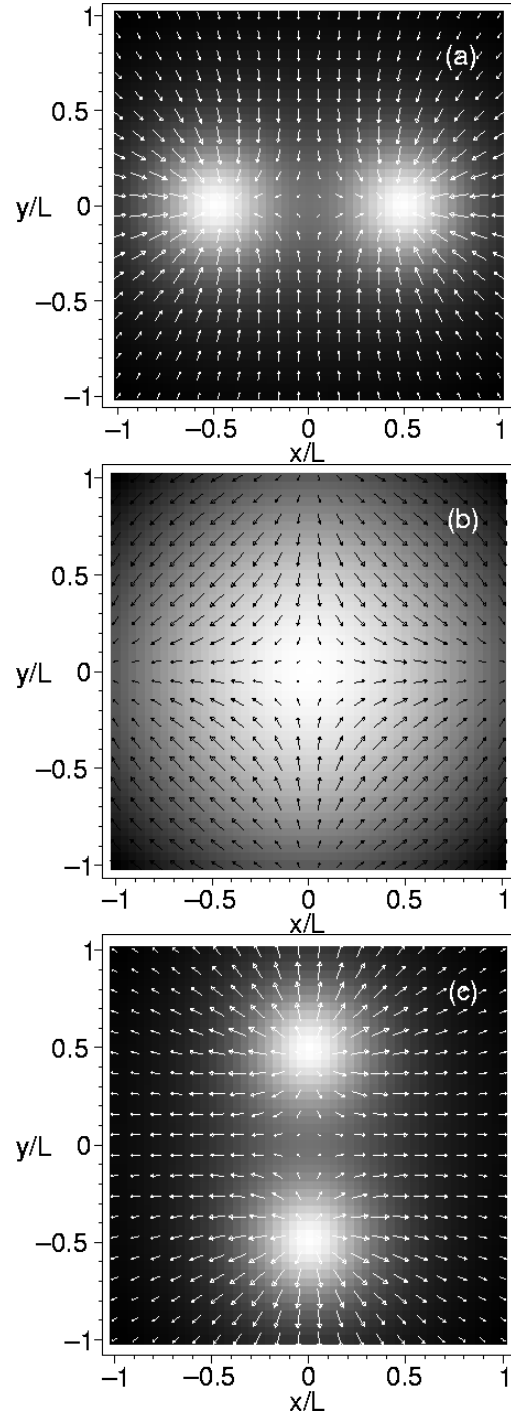


Fig. 2.— The effective magnetograms of the model configuration at  $l/L = 0.5$ ,  $d/L = 0.4$  in the planes  $z = L$  (a),  $z = 0$  (b) and  $z = -L$  (c). The distribution of the  $B_{0z}$ -component is shown in grey half-tones, while vectors represent the transverse magnetic field. The intensity of the grey half-tones and the length of the vectors are normalized by the corresponding maximum values in the planes.

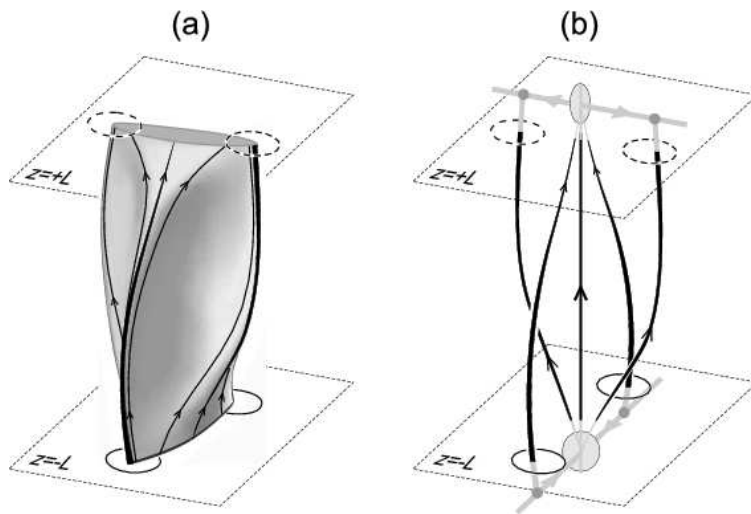


Fig. 3.— The HFT in a simplified configuration (a) and the topological structure of the field including the fictive magnetic charges and nulls which are located outside the model volume. The circles in the planes  $z = \pm L$  represent the sunspots, while the grey circles (b) show the separatrix fan planes at the nulls, from where the separatrix spine lines emanate towards the charges. The varying thickness of the field lines depicts the corresponding variation of the field strength or their “rigidity”.

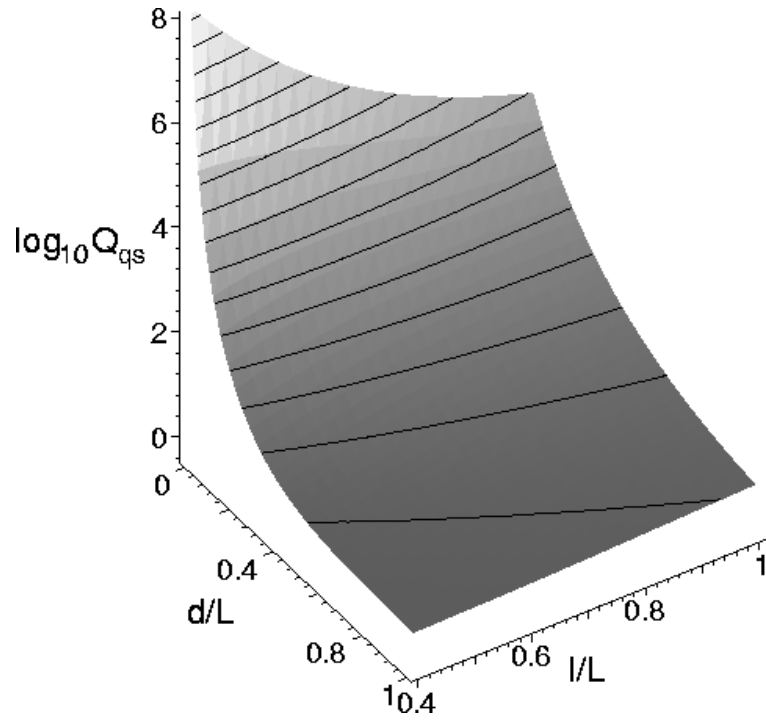


Fig. 4.— The logarithm of the squashing degree  $Q_{qs}$  at the quasi-separator as a function of the depth  $d$  and half-distance  $l$  between the sources. The length scales are normalized to the half-length  $L$  of the HFT and the equidistant contours are plotted with an increment of 0.5.

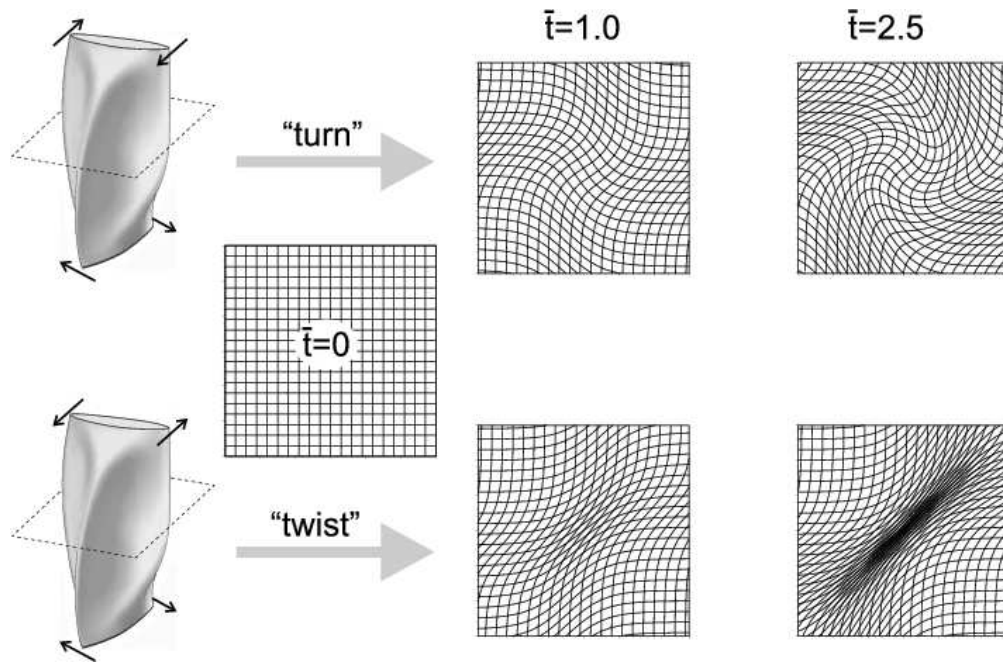


Fig. 5.— Non-pinching (top) and pinching (bottom) deformations of the HFT in the (dash-outlined) plane  $z = 0$  due to “turning” and “twisting” shearing motions, respectively, applied to the HFT feet.

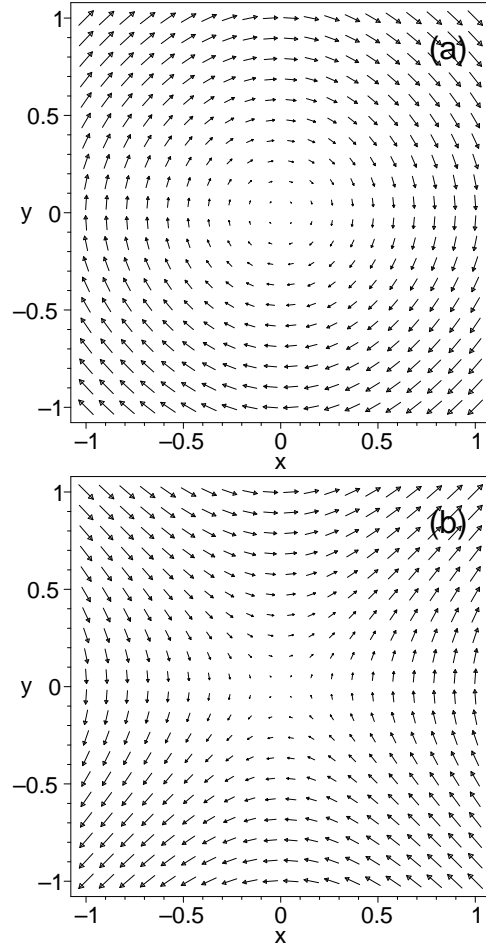


Fig. 6.— Rotational (a) and hyperbolic (b) velocity fields in the plane  $z = 0$  due to “turning” and “twisting” shearing motions, respectively, applied to the HFT feet.



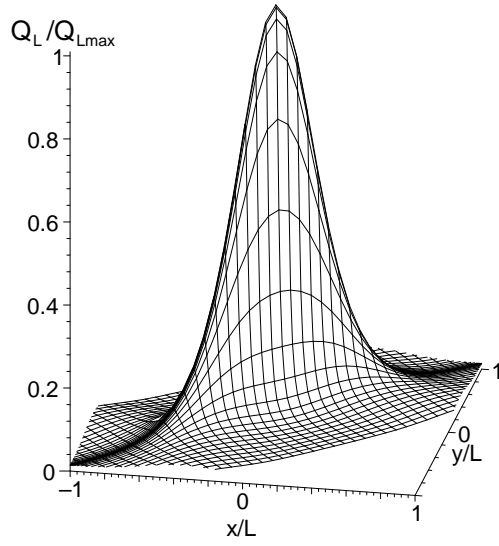


Fig. 7.— The degree of squashing  $Q_L$  of Lagrangian plasma elements in the plane  $z = 0$  at  $\bar{t} = 2.5$  (other parameters:  $d/L = 0.4$  and  $l/L = 0.5$ ) for the deformation caused by the “twisting” photospheric shearing motion.

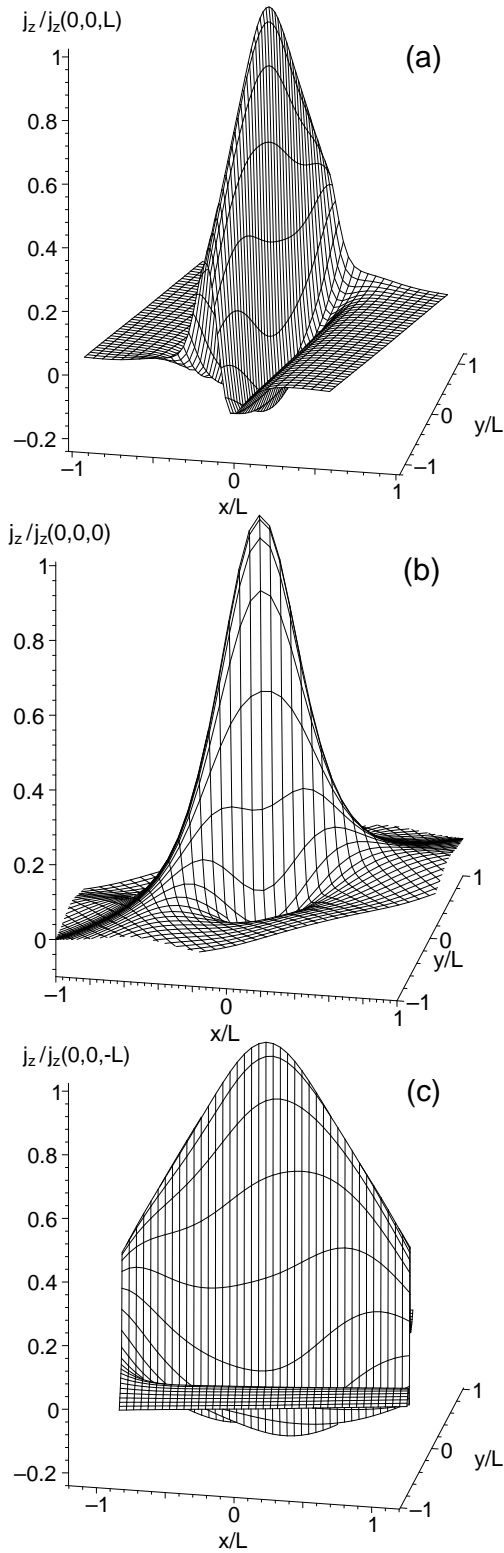


Fig. 8.— The distribution of the current density  $j_z$  in the planes  $z = L$  (a),  $z = 0$  (b) and  $z = -L$  (c) at  $\bar{t} = 2.5$  for the deformation due to the “twisting” photospheric shearing motion ( $d/L = 0.4$  and  $l/L = 0.5$ ).

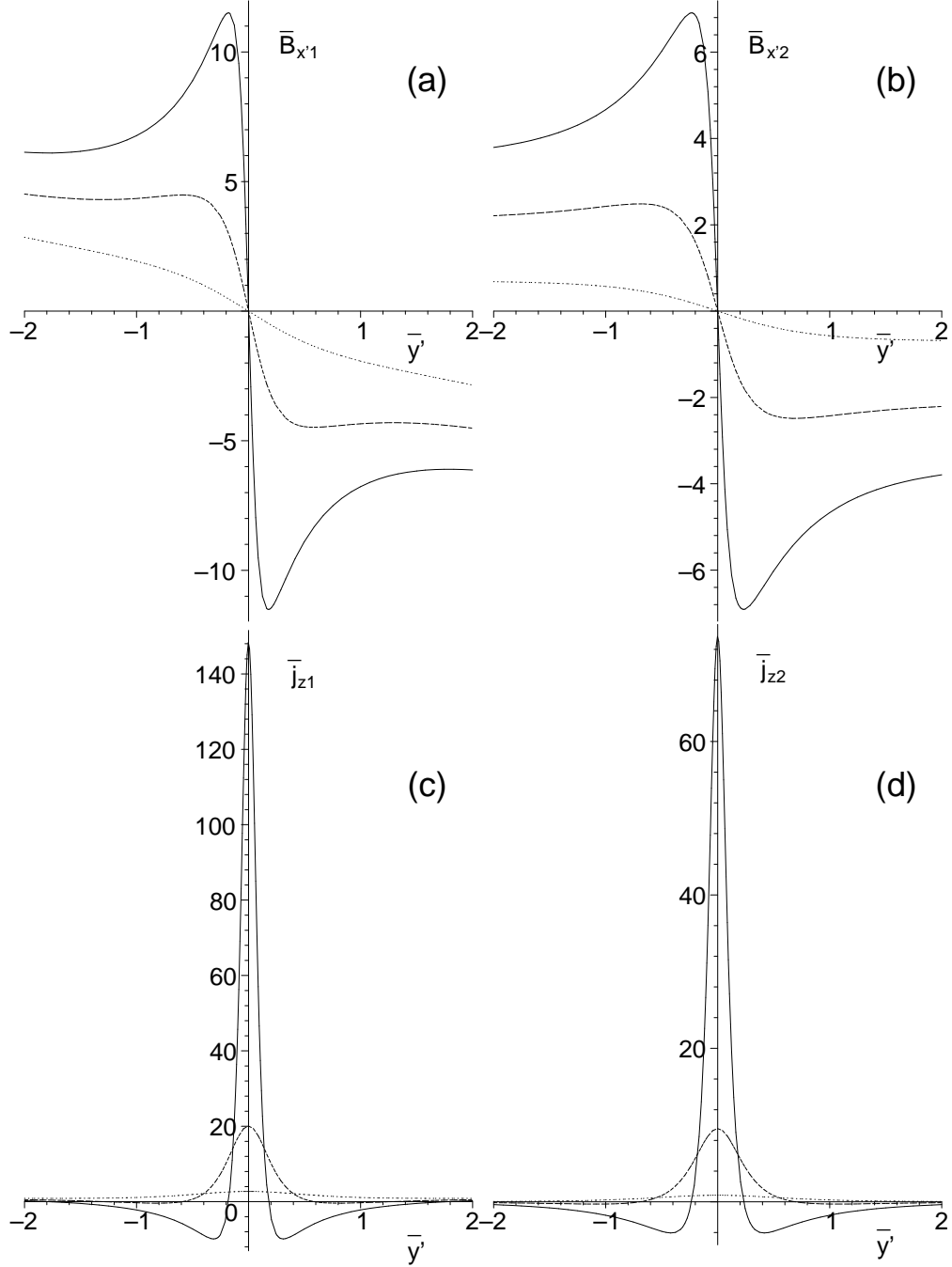


Fig. 9.— The magnetic fields  $\bar{B}_{x'1}$  and  $\bar{B}_{x'2}$  (a, b) normalized to  $hl_{\text{sh}}$  and  $B_{\parallel}l_{\text{sh}}/L$ , respectively, and the corresponding current densities  $\bar{j}_{z1}$  and  $\bar{j}_{z2}$  (c, d) normalized to  $h/\mu_0$  and  $B_{\parallel}/(\mu_0L)$ , respectively, at  $x' = z = 0$ . Dotted, dashed and solid lines correspond to  $\bar{t} = 0.5$ , 1.5 and 2.5, respectively.

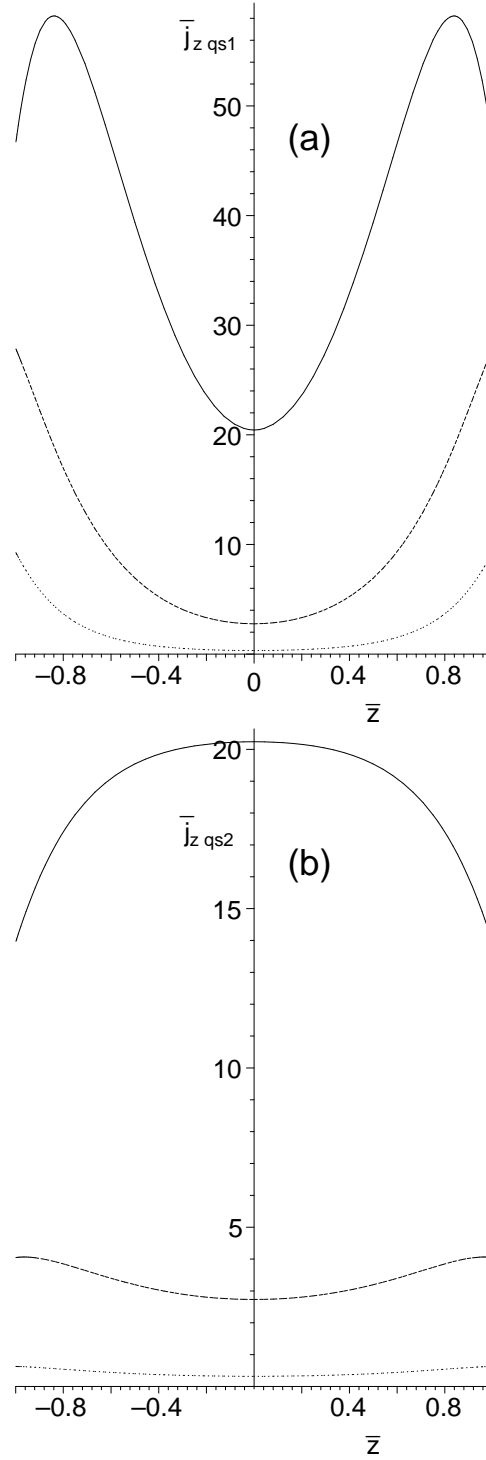


Fig. 10.— The distributions of current densities  $\bar{j}_{z\text{ qs1}}$  and  $\bar{j}_{z\text{ qs2}}$  normalized to  $B_s/(\mu_0 L)$  along the quasi-separator ( $\bar{z} = z/L$ ) for the same parameter values as used in Figure 2. Dotted, dashed and solid lines correspond to  $\bar{t} = 0.5, 1.5$  and  $2.5$ , respectively.

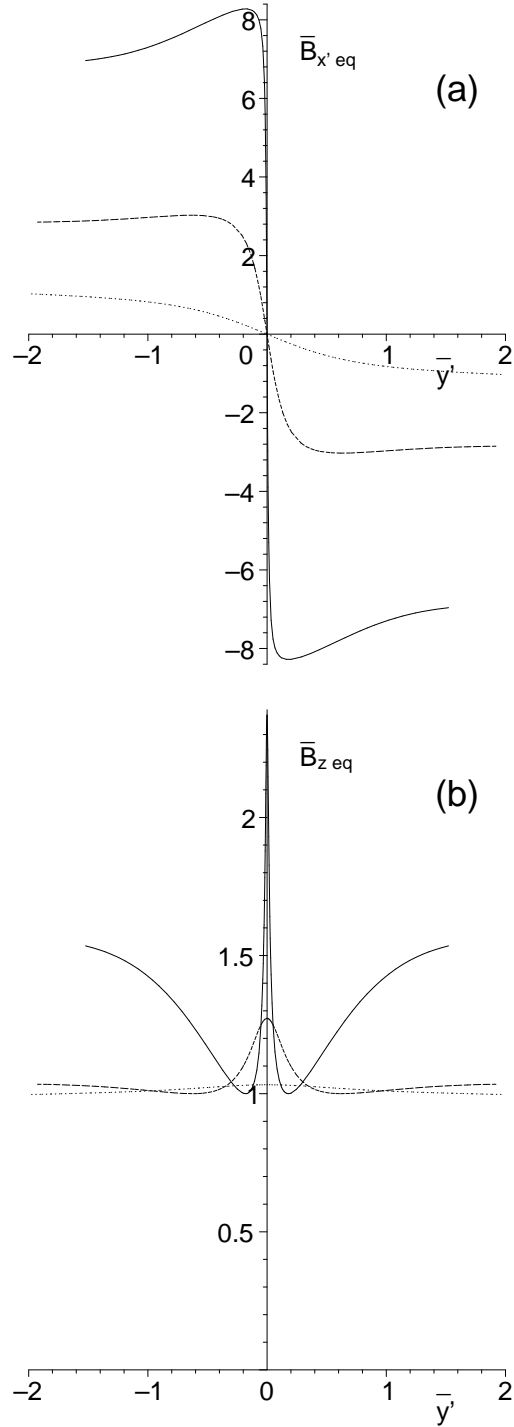


Fig. 11.— The profiles of the equilibrium field components  $B_{x'eq}$  and  $B_{z eq}$  normalized to  $B_{\parallel}l_{sh}/L$  and  $B_{\parallel}$ , respectively, for the same parameter values as used in Figure 2. Dotted, dashed and solid lines correspond to  $\bar{t} = 0.5, 1.5$  and  $2.5$ , respectively.

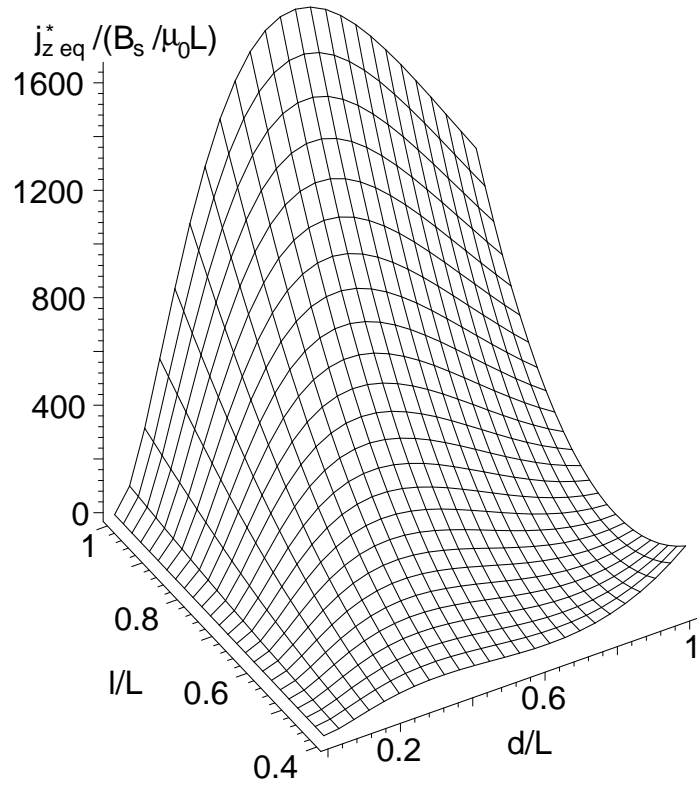


Fig. 12.— The equilibrium current density  $j_{z \text{ eq}}^*$  at  $\mathbf{r} = 0$  and  $\bar{t} = 2.5$  versus the model parameters  $l/L$  and  $d/L$ .